





Speed of fragments ejected by an expanding liquid tin sheet

Bo Liu ^{1,2} Javier Hernandez-Rueda ^{1,*} Hanneke Gelderblom ³ and Oscar O. Versolato ^{1,2,†}

¹*Advanced Research Center for Nanolithography (ARCNL), Science Park 106,
1098 XG Amsterdam, The Netherlands*

²*LaserLab, Department of Physics and Astronomy, Vrije Universiteit Amsterdam, De Boelelaan 1105,
1081 HV Amsterdam, The Netherlands*

³*Fluids and Flows group, Department of Applied Physics, Eindhoven University of Technology, Den Dolech 2,
5600 MB Eindhoven, The Netherlands*



(Received 4 April 2022; accepted 3 August 2022; published 29 August 2022)

We experimentally investigate the speed of fragments produced by ligament breakup in the laser-induced deformation of tin microdroplets into axisymmetric sheets. The experiments were carried out covering a wide range of droplet diameters and laser-pulse energies. In addition to fragments produced by end-pinching, we also observe fragments shed via Rayleigh-Plateau breakup of long ligaments at late times. A double-frame backlit camera was used to obtain the speeds of the fragments u_f and the time of their detachment t_d . We show that by normalizing u_f to the initial expansion speed of the sheet \dot{R}_0 , all data collapse onto a single, universal curve that is a function of the dimensionless time t_d/τ_c only, where τ_c is the capillary time. This universal curve is explicitly independent of the droplet's Weber number. The collapse of u_f is supported by energy conservation arguments. Our findings enable the prediction of the instantaneous speed and position of the fragments shed from liquid tin targets used in state-of-the-art extreme ultraviolet nanolithography, facilitating the design of effective mitigation strategies against microparticulate debris.

DOI: [10.1103/PhysRevFluids.7.083601](https://doi.org/10.1103/PhysRevFluids.7.083601)

I. INTRODUCTION

Liquid fragmentation caused by the impact of droplets is a ubiquitous process in nature that is important in numerous industrial applications. In agriculture, the efficiency of the uptake of nutrients by the leaves of a plant is affected by the splashing that originates from the impact of droplets in pesticide sprays [1]. In the case of airborne-transmitted diseases, fragments of liquid that originate from the respiratory system of animals can travel a long distance and transport biological agents [2–4]. In the semiconductor industry, splashing and fragmentation processes also play a key role [5,6]. Modern sources of extreme ultraviolet (EUV) light for nanolithography use liquid tin to generate EUV light with a wavelength centered at 13.5 nm in a two-step process [7–11]. In the first step, a ns-laser prepulse illuminates a spherical microdroplet of liquid tin, inducing its propulsion and deformation into an expanded target consisting of a thin sheet and a rim that bounds the perimeter of the sheet [12,13]. This target is subsequently irradiated by a second laser main-pulse

*Present address: Departamento de Óptica, Facultad de Ciencias Físicas, Universidad Complutense de Madrid, Plaza de Ciencias 1, 28040 Madrid, Spain.

†versolato@arcnl.nl

Published by the American Physical Society under the terms of the [Creative Commons Attribution 4.0 International](https://creativecommons.org/licenses/by/4.0/) license. Further distribution of this work must maintain attribution to the author(s) and the published article's title, journal citation, and DOI.

to produce a hot and dense plasma that emits EUV light [14–18]. The droplet deformation driven by the prepulse also results in the generation of micron-sized fragment “debris,” which may drastically reduce the lifetime of the collection optics within the commercial sources of EUV light [5,19–21]. Therefore, a thorough understanding of the shedding mechanism of fragmentation in the context of laser-pulse impact on a droplet is highly relevant to optimize the performance and to extend the lifetime of EUV sources.

To better understand the physics that dictates the fragmentation of tin droplets after prepulse irradiation, we draw on analogies to canonical cases of droplets impacting onto solid substrates. Such analogies were made in prior experimental work by Klein *et al.* [5,22] and in a theoretical study by Gelderblom *et al.* [23] to describe the deformation and fragmentation of a sheet produced from a laser-pulse-impacted droplet. Upon impact, a droplet deforms into a thin sheet, bounded by a thicker rim. The liquid contained in the sheet flows outward towards the periphery, progressively increasing the mass content of the bounding rim [24]. Due to the restoring force exerted by the surface tension, the rim continuously decelerates. On the other hand, the fluid particles on the sheet follow ballistic radial paths since there are only weak pressure gradients along the radial direction [2,24]. Once coalesced with the decelerating rim, the velocity of the liquid flowing from the sheet suddenly decreases [24]. This rapid change in speed leads to an increase of the static pressure and to a loss of total energy [24]. In addition, the gradual deceleration of the rim leads to Rayleigh-Taylor (R-T) instabilities, which, combined with the Rayleigh-Plateau (R-P) instabilities, cause azimuthal undulations that ultimately aggregate into ligaments fed by the pressurized liquid contained in the rim [5,24,25]. Finally, the ligaments break into fragments via ligament pinch-off. The produced fragments have a speed u_f which equals the speed of the corresponding ligament tip at one necking time prior to the pinch-off [2]. Overall, the fragmentation dynamics is the result of a complex interplay of local rim destabilization and flow in the sheet, set in motion by the impact of the droplet.

While splashing and fragmentation processes related to the impact of droplets on solids have been widely studied, it is surprising that only a few studies deal with the velocity of the produced fragments. Riboux *et al.* [26,27] and Thoroddsen *et al.* [28] investigated the speed of fragments produced by the impact of mm-sized water droplets on a large solid surface. These works, however, focused on the initial stage of the fragment’s behavior shortly after impact at $t \ll t_i$, where $t_i = D_0/U$ is the inertial time with D_0 and U the diameter and the initial speed of the impacting droplet, respectively. In these cases, the distribution of fragment size and velocity are influenced by the capillary force and the viscous stress at the lamella in contact with the surface. These effects on the fragmentation process are expected to depend on the area of the solid on which the droplet impacts. Inspired by the splashing effects occurring close to the edge of plant leaves, Wang *et al.* [2] investigated the impact of mm-sized droplets on a pillar with a diameter similar to the droplets, studying the speeds of fragments as shed from the growing and retracting sheet. They found experimental evidence of a self-similar behavior of the speed of fragments, later supported by an analytical work in Ref. [29]. In the case of tin microdroplets irradiated with a laser pulse, it is the violent expansion of the laser-produced plasma near the droplet surface that provides a recoil pressure with a magnitude of 100 kbar [23,30–32], which results in an effectively instantaneous (~ 10 ns $\ll t_i$) momentum kick leading to propulsion and expansion velocities on the order of 100 m/s [30–32]. In this extreme context, where time and spatial dimensions significantly differ from those found in droplet-impact-on-solid cases, the interplay of the parameters that condition the speed of fragments is not obvious. The absence of a rigid surface implies that there is no solid contact—there is no impactor. This difference in the boundary conditions will influence the fluid dynamic response of the droplet [23], modifying the evolution of the sheet and its thickness [12,13,23,33]. Furthermore, different magnitudes of initial perturbations, when comparing water and tin laser-impacted droplet systems, appear to induce disparities in the capillary instabilities that govern the breakup of the sheet [5,34]. The influence of the amplitude of such initial perturbations on the speed of shed fragments is unknown. Therefore, there is a need for a systematic study of the speed of fragments induced by a laser impact on tin microdroplets.

In this paper, we experimentally investigate the speed u_f of fragments that result from the laser-induced deformation of tin microdroplets. We include droplets with different diameters D_0 impinged by laser pulses of various energies E_p , which enables us to cover a wide range of Weber numbers and relevant timescales. We employ stroboscopic microscopy using a double-frame camera to capture the ballistic trajectory of fragments shed from ligaments protruding from the rim. Our imaging systems, with the optical resolution enhanced with respect to our previous studies, allow observations of fragments shed from ligaments not only by the canonical end-pinching mode, but also by a R-P instability occurring on those long ligaments that appear at later moments. Our benchmark studies of the dynamics of the sheet's expansion and contraction underscore the validity of using a global deformation Weber number to characterize these dynamics following Ref. [5]. Next, we present the results of our measurements of fragment speed u_f and the dependence thereof on detachment time t_d and Weber number. The speed of the fragments is shown to always exceed the instantaneous expansion velocity of the rim \dot{R}_r , where the difference $u_f - \dot{R}_r$ increases with time, starting at zero at the onset of the impact, i.e., $u_f \rightarrow \dot{R}_r$ at $t_d \rightarrow 0$. Furthermore, we show that normalizing u_f to the initial expansion speed \dot{R}_0 provides a universal curve u_f/\dot{R}_0 that is a function of the dimensionless time t_d/τ_c only and is independent of the Weber number. This self-similar behavior of u_f is demonstrated to be supported by energy conservation arguments when considering the fraction of the total energy taken by the fragmentation channel.

II. EXPERIMENTAL SETUP

Figure 1(a) presents a schematic top-view of the experimental setup. A detailed description of the subsystems of the setup can be found in Refs. [12,30]. The laser-tin interaction experiments are carried out in a vacuum chamber (10^{-7} mbar) with several ports that provide optical access. A tin reservoir is situated on top of the chamber and is kept at a constant temperature of 260°C that is well above the melting point of tin (234°C [35]). From the reservoir, a droplet generator dispenses a vertically aligned train of liquid tin microdroplets, which retain the initial 260°C temperature during their in-vacuum flight with liquid density $\rho = 7000\text{ kg/m}^3$, surface tension $\sigma = 0.54\text{ N/m}$, and dynamic viscosity $\mu = 1.8 \times 10^{-3}\text{ Pa s}$ [36,37]. In the experiments, we systematically investigate droplets with five diameters $D_0 = 27, 34, 39, 43, \text{ and } 67\ \mu\text{m}$. A few millimeters above the center of the chamber, the droplet stream passes through a horizontal light sheet produced by a helium-neon (He-Ne) laser. The light scattered by the droplets is detected by a photomultiplier tube (PMT), providing a signal with a repetition rate on the order of kHz. This signal is down-converted to 10 Hz, sent to a delay generator and used to trigger the data acquisition and laser systems.

Once a droplet reaches the center of the chamber, it is irradiated by a circularly polarized laser-pulse at 1064 nm with a pulse duration of 10 ns at full width at half maximum (FWHM). The laser pulses are delivered by a Nd:YAG laser system (Quanta-Ray, Spectra-Physics). The laser is focused to a Gaussian-shaped beam profile with a diameter $\approx 135\ \mu\text{m}$ (FWHM) at the surface of the droplets. We employed two different laser pulse energies for each droplet size, enabling us to cover a wide range of the relevant Weber number, which ranges from approximately 1100 to 5500. In our experiments, the Ohnesorge number $\text{Oh} = \mu/\sqrt{\rho\sigma D_0} \sim 10^{-3}$, which indicates a negligible influence of viscosity to the impact dynamics compared to the surface tension. The droplet capillary timescale $\tau_c = \sqrt{\rho D_0^3/(6\sigma)}$ ranges from 6.5 to 25 μs . Detailed experimental conditions and the parameters derived are summarized in Table I in the Appendix.

The expansion and fragmentation dynamics of the sheet are inspected using a stroboscopic shadowgraphy imaging system, which consists of long-distance microscopes (K2 DistaMax, Infinity Photo-Optical) attached to CCD cameras. We record the droplet dynamics at 90° and 30° with respect to the laser propagation direction, as shown in Fig. 1(a), thus obtaining side- and front-view images, respectively. The imaging systems use incoherent light pulses at $560 \pm 10\text{ nm}$ with a pulse duration of 5 ns (FWHM) to provide the backlighting of the image. These probe pulses are generated within rhodamine 6G dye cells that are pumped with 532-nm-pulsed laser light. The side-view system uses a CCD camera (Manta G145-B, AVT), which utilizes a CF-1/B objective

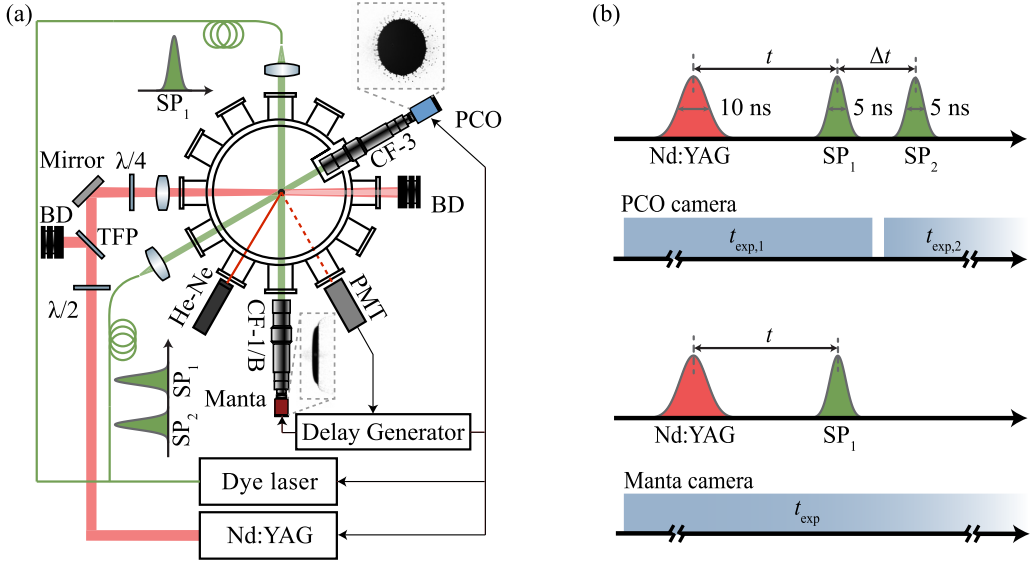


FIG. 1. (a) Top-view schematic of the experimental setup including a vacuum chamber, synchronization and trigger systems, Nd:YAG drive laser, and imaging systems. During the experiments, individual liquid tin microdroplets are irradiated by single ns-laser pulses. The energy of the laser pulse is controlled by using a half-wave plate and a thin-film-polarizer (TFP). The beam is dumped in a beam dump (BD). A quarter-wave plate is used before the final focusing lens to set a circular polarization. The imaging systems employ a double-frame CCD camera (PCO-4000) and a single-frame CCD camera (AVT Manta B145-G), which provide front- and side-view images of the expanding tin sheet at 30° and 90° with respect to the laser direction, respectively; see inset example front- and side-view shadowgraphy images as recorded by the PCO and Manta cameras. Two consecutive shadowgraphy probe pulses SP_1 and SP_2 are used as illumination sources for the front-view microscope, whereas a single pulse SP_1 is used for the side-view system. (b) Time sequence of the illumination pulses and their relation with the much longer exposure windows of the cameras. The time $t = 0$ sets the moment at which the drive laser pulse illuminates a droplet. At a time delay t , the first probe pulse SP_1 illuminates the expanding tin, overlapping with the exposure windows of both PCO cameras ($t_{\text{exp},1}$) and Manta (t_{exp}). After SP_1 , the second probe pulse SP_2 is collected by the PCO camera at $t + \Delta t$, within the second exposure window $t_{\text{exp},2}$. The full temporal span of the target dynamics is obtained by scanning the time delay t .

(Infinity Photo-Optical) and captures single frames generated by a single shadowgraphy probe pulse SP_1 during the exposure of the camera t_{exp} . The front-view microscope is equipped with an CF-3 objective (Infinity Photo-Optical) with a shorter working distance for an increased resolution ($\sim 3 \mu\text{m}$), and is set up at a distance of 110 mm from the target sheet. This microscope uses a camera (PCO-4000) capable of acquiring two consecutive frames of the same tin sheet with an effective minimum interframe delay of 280 ns. This double-frame camera captures two consecutive probe pulses SP_1 and SP_2 with a relative time delay Δt , which is tunable and typically ranges from 1 to $5 \mu\text{s}$ in the experiments. The time sequence of the probe pulses SP_1 and SP_2 and the corresponding exposure windows of the camera, $t_{\text{exp},1}$ and $t_{\text{exp},2}$, are shown in Fig. 1(b).

III. LIGAMENT BREAKUP

Figure 2 presents a set of high-resolution front-view images collected in this study that illustrates the sheet expansion at different time delays. In this specific case, a droplet with an initial diameter of $D_0 = 67 \mu\text{m}$ was irradiated using a laser pulse with an energy of $E_p = 7 \text{ mJ}$. After laser excitation, the droplet is propelled along the laser propagation direction and deforms into an axisymmetric sheet, which expands, contracts, and fragments over time. The expansion and propulsion of the

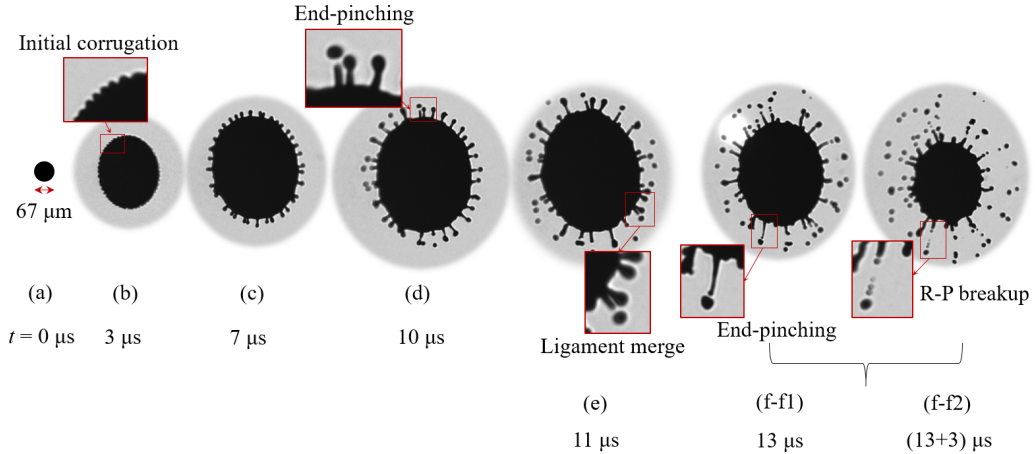


FIG. 2. Front-view shadowgraphy images of the laser-induced tin sheet expansion and fragmentation at different time delays t , where $t = 0$ marks the onset of the ns-laser impact [each time delay, from panel (a) to (f-f1), corresponds to a different laser-droplet impact event]. These images were obtained using droplets with a diameter of $D_0 = 67 \mu\text{m}$ and a laser pulse energy of $E_p = 7 \text{ mJ}$. (a) Shadowgraphy image of a droplet right before laser exposure at $t = 0$, which serves as scale bar. (b) At $t = 3 \mu\text{s}$, the droplet promptly expands into an axisymmetric sheet, with an initial expansion rate of $R_0 \approx 38 \text{ m/s}$. The inset provides a zoom of the emergent rim corrugations. (c) At $t = 7 \mu\text{s}$, corrugations further develop into ligaments. (d) At $t = 10 \mu\text{s}$, fragments are shed via end-pinching, further illustrated in the inset zoom-in. (e) At $t = 11 \mu\text{s}$, some ligaments merge together (also see zoom-in inset). (f-f1) At $t = 13 \mu\text{s}$, ligaments have grown to a typical length of several tens of micrometer. The inset illustrates the formation of a fragment that has just detached from the tip of a ligament with a length of $\approx 50 \mu\text{m}$. (f-f2) The very same sheet shown in (f-f1), but $3 \mu\text{s}$ later. The inset shows the same ligament as in (f-f1) here breaking into several fragments via R-P instability.

droplet are induced by the recoil pressure that results from the violent expansion of a laser-produced plasma (see, e.g., Refs. [12,22,23,30]). As the sheet expands, a rim forms at the perimeter of the sheet, typically reaching a rim thickness of several micrometers, as reported in Refs. [12,13]. Shortly after the formation of the rim, it destabilizes due to the combined effect of R-T and R-P instabilities that progressively enhances any initial perturbation on the rim to visible corrugations [24,25].

Figure 2(b) taken at $t = 3 \mu\text{s}$ shows the initial corrugations a fraction of which [5,38] further develop into ligaments that grow along the radial direction, as we illustrate in Fig. 2(c) at $t = 7 \mu\text{s}$. Tin from the sheet continuously feeds the base of the ligaments, and thus these grow over time and ultimately break into small fragments. This breaking process is first dominated by *end-pinching* [2], shedding one droplet at a time as illustrated in Fig. 2(d) at $t = 10 \mu\text{s}$. The inset shows an enlarged picture to exemplify the end-pinching event. We observe that the onset of fragment generation decreases with increasing Weber number. A detailed analysis will feature in a forthcoming work. Later on, the ligaments merge [see Fig. 2(e)] and stretch, reaching lengths of several tens of micrometers. Figure 2(f-f1) at $t = 13 \mu\text{s}$ shows such a long ligament, with a length of approximately $50 \mu\text{m}$. At this stage, the fragments are generated not only via end-pinching, but also via *R-P breakup*, where multiple droplets are produced nearly simultaneously. Such a ligament breakup event is presented in the insets of Figs. 2(f-f1) and 2(f-f2), which illustrate the evolution of the exact same ligament with over a time interval $\Delta t = 3 \mu\text{s}$ as recorded by our double-frame camera. The ligament shown in the insets exhibits both an end-pinching event in Fig. 2(f-f1) and a R-P breakup in Fig. 2(f-f2).

Ligament breakup via R-P instability

To explain the occurrence of both the end-pinching and R-P breakup modes, we now discuss the relevant dynamics of the ligaments in more detail. Wang *et al.* [38], in their work on

droplet-pillar impact, reported on ligaments breaking into fragments via end-pinching. They did not observe ligaments growing into long liquid jets required for the R-P breakup mode. The absence of this second mode of breakup was explained in the context of a critical Weber number We_c [38] which was originally introduced by Clanet *et al.* [39] for the flow out of a stationary orifice and was later refined by Ambravaneswaran *et al.* [40]. For droplet impact, at small ligament Weber numbers $We_l = \rho u_l^2 w_l / \sigma < We_c$, fragments form from ligaments solely via end-pinching; here u_l is the ligament speed in the comoving frame following the expansion of the rim and w_l is the mean diameter of the ligament [38]. For cases $We_l > We_c$, we expect the transition from end-pinching to jetting to occur. Here, long ligaments are formed which break into multiple droplets via R-P instabilities [38,41].

In our experiments, we observe that end-pinching governs the ligament breakup for the dominant fraction of the studied time interval. At late times, however, we clearly see the formation of long ligaments which break up via R-P instabilities, i.e., a transition from end-pinching to jetting occurs. This transition is expected considering the analytical prediction from Ref. [38], which indicates a monotonic increase of We_l and a decrease of We_c with increasing t/τ_c , independent of the droplet's Weber number. As a corollary, the criterion of $We_l \sim We_c$ will be met at some constant time t/τ_c , which is analytically given as $t \approx 0.76\tau_c$, as can be derived from Ref. [38]. The transition to jetting appears to occur earlier in our experiments, cf. the example case shown in Figs. 2(f-f1) and 2(f-f2) where the R-P breakup related to jetting starts to become visible around $t \approx 13 \mu\text{s} \approx 0.5 \tau_c$. This observation of an earlier transition to jetting should be compared to the fact that our experiments exhibit an earlier apex time t_{max}/τ_c of the sheet expansion (see below) and a faster expansion rate in the early stages. Therefore, the growth of We_l that is set by the sheet expansion will be faster and may thus be expected to reach the critical Weber number at an earlier time, in line with our observations of R-P breakup.

IV. SHEET EXPANSION

Figure 3(a) presents a front-view shadowgraphy image of an example sheet, which we use to illustrate the steps taken to determine the radius of the sheet's rim R_r and the radial position of the ligaments R_l . In this section, we will first discuss the expansion trajectory of the rim radius R_r ; the ligament radius R_l will be separately discussed in Sec. VB. The image in Fig. 3(a) was recorded $8 \mu\text{s}$ after illuminating a tin droplet ($D_0 = 67 \mu\text{m}$) with a laser pulse ($E_p = 20 \text{mJ}$). In line with the method used in Ref. [38], we first locate the outer contour that bounds the ligaments on the sheet perimeter [see the red lines in Fig. 3(a)]. We then locate the inner contour — which is retrieved as the baseline of the outer contour — as the position of the rim [see the blue lines in Fig. 3(a)]. The radius of the rim R_r is thus defined as the radial distance from the inner contour to the center of the sheet. Due to the axisymmetric geometry of the sheet, R_r does not show angular fluctuations: our data shows a small 2 to 4% variation over the relevant angular interval. We can then identify R_r as the average radius of the rim along the sheet's perimeter.

Figure 3(b) presents the rim radius R_r as a function of time for the same experimental conditions as used for Fig. 3(a). In Fig. 4, we further plot the results for $R_r(t)$ for all data available as summarized in Table I. For a given parameter set, we record a stroboscopic time series by performing a single laser experiment for each time delay t between laser impact and the illumination pulse (see Fig. 1). To ensure the reliability and repeatability of our results, we perform 20–50 impact events per parameter set for each time delay. The uncertainties shown in Figs. 3(b) and 4(a) equal the standard deviation of the measurement ensembles. In Fig. 4(a), for a fixed droplet size, we observe a faster initial expansion and a larger apex radius of the sheet R_{max} when increasing the laser energy. We also observe that the apex time t_{max} (at which the sheet reaches R_{max}) increases with the droplet size. After reaching R_{max} , the sheet starts to shrink due to the surface tension. In Ref. [38], a collapse of R_r onto a universal curve was reported, captured by the function $y = f(x)$ with variables $x = t/\tau_c$ and $y = R_r D_0^{-1} We^{-1/2}$ where $We = \rho U^2 D_0 / \sigma$ is the Weber number with U the impact speed. An earlier work by Villermaux *et al.* [24] suggested a similar collapse of R_r by

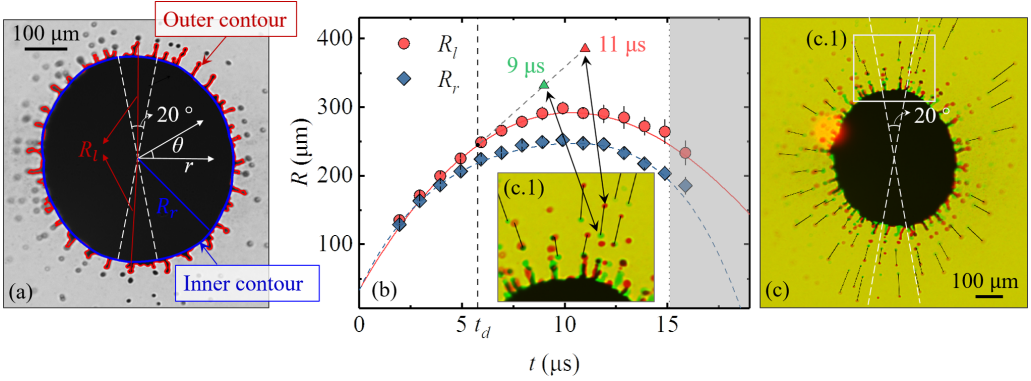


FIG. 3. (a): Front-view shadowgraphy image (horizontally stretched to correct for the 30° observation angle) of an expanding tin sheet to illustrate the radial position of the sheet's rim R_r (blue inner contour) and the ligaments R_l (red outer contour). On the same image, we overlay a polar coordinate system (r, θ) with its origin at the center of the sheet. The picture was taken $8 \mu\text{s}$ after illuminating a $D_0 = 67 \mu\text{m}$ droplet with a $E_p = 20 \text{ mJ}$ laser pulse. We restrict the ligament and fragment analysis to the region (see the main text) comprising $\theta = 90^\circ \pm 10^\circ$ and $270^\circ \pm 10^\circ$ (dashed white lines). Within this azimuthal range, the longest ligaments originating from the top and bottom of the sheet are highlighted by their radial positions R_l . (b) Expansion trajectory of the ligaments from the top side R_l (red circles) and the rim R_r (blue diamonds) as a function of time. The solid curve presents a polynomial fit to the R_l data. The dashed line presents a polynomial fit to R_r data. The shaded area indicates the time regime $t > 0.6\tau_c (= 15.1 \mu\text{s}$ for $D_0 = 67 \mu\text{m})$ that is excluded in the fitting as sheet breakup may hinder accurate tracking of R_r . (c) Postprocessed shadowgraphy images captured at $t = 9$ and $11 \mu\text{s}$ by the double-frame camera, overlapped with respect to the sheet's center. Black pixels indicate overlap regions, where tin is present in both frames. Yellow pixels account for the background in the absence of tin. Green and red pixels indicate the presence of tin at either 9 or $11 \mu\text{s}$, respectively. The black lines connecting the same green- and red-colored fragments illustrate their ballistic trajectory over the $2 \mu\text{s}$ time interval. The inset (c.1) shows a close-up of the ballistic trajectory of fragments. One example of a fragment trajectory is highlighted with its position at $t = 9$ and $11 \mu\text{s}$, linked to the data markers in panel (b). The intersection between the fragment's trajectory in panel (b) and ligament expansion curve R_l is used to determine the detachment time t_d as indicated by a vertical line.

scaling $y = (R_r - R_0)D_0^{-1}We^{-1/2}$ and $x = t/\tau_c$, which is equivalent to the collapse proposed by the authors of Ref. [38] when $We \gg 1$, applicable in our cases (see Table I). In line with Ref. [38], we plot the data of R_r upon rescaling in terms of the similarity variables in Fig. 4(b). The speed used in the Weber number in this panel is the center-of-mass speed U of the sheet along the laser pulse direction. This speed is determined by measuring the displacement of the sheet's center-of-mass over a finite time interval (typically over a few microseconds) using side-view images (for further details see Refs. [22,30,31]). It is evident that the normalization of t/τ_c successfully collapses the apex time t_{max} . However, normalizing rim radii by the impact Weber number results in a systematic disparity between the lower energies group (open symbols) and the higher energies (full symbols). Therefore, the center-of-mass speed does not characterize the expansion dynamics of the droplet for the full range of droplet sizes and pulse energies. In the case of droplet impact onto a pillar, the initial expansion rate of the droplet $\dot{R}_r(t=0)$ (referred to as \dot{R}_0 hereafter) may deviate from the orthogonal speed of the impact U when varying the size of the drop relative to the pillar diameter [2,24,33,38]. Villermaux *et al.* [24] analytically proposed and further experimentally confirmed that $\dot{R}_0 = U$ under their experimental conditions. Wang *et al.* in Ref. [29], however, observed a much larger deformation speed of $\dot{R}_0 \approx 2U$. The physics origin of the factor of 2 difference between U and \dot{R}_0 in the latter case is not yet clear [29]. In case of laser-induced deformation, the correlation between the two orthogonal speeds \dot{R}_0 and U is well understood. This correlation is jointly determined by the droplet size, the laser pulse energy, and the beam profile and was shown to be captured by a single

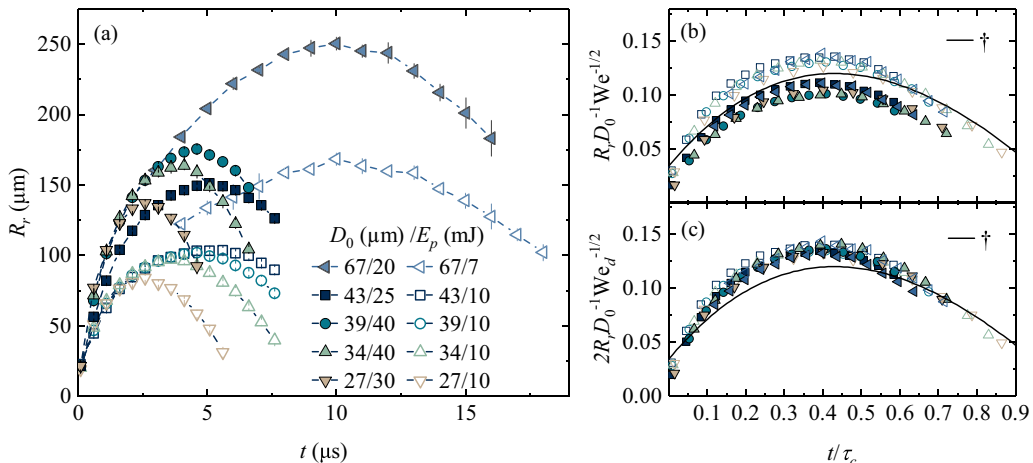


FIG. 4. (a) Rim radius R_r as a function of time t for several D_0 - E_p combinations. The error bars represent the standard deviation of the binned data. (b) Scaled rim radius, $R_r D_0^{-1} \text{We}^{-1/2}$, as a function of the non-dimensional time t/τ_c , with $\text{We} = \rho U^2 D_0 / \sigma$ and τ_c the capillary time. (c) Scaled rim radius $2R_r D_0^{-1} \text{We}_d^{-1/2}$ as a function of t/τ_c , where the deformation Weber number is $\text{We}_d = \rho \dot{R}_0^2 D_0 / \sigma$. Solid lines in (b) and (c) show the solution for R_r from Ref. [29] (\dagger). The error bars were omitted both in (b) and (c) for better visibility.

dimensionless pressure impulse width exerted by the plasma on the surface of the droplet (for details see Refs. [23,32]). In brief, the expansion speed \dot{R}_0 monotonically increases with increasing U and is of the same order: $\dot{R}_0 \sim U$. A narrower pressure impulse width leads to a larger ratio of \dot{R}_0/U [23]. Typically, an increase in laser pulse energy leads to a reduction of \dot{R}_0/U [5,32]. In the current study, this ratio varies from 1.4 to 1.8 over the studied range of droplet sizes and pulse energies. The authors of Refs. [5,13] further demonstrated that it is the expansion speed \dot{R}_0 that should be taken as the characteristic speed, defining the *deformation* Weber number $\text{We}_d = \rho \dot{R}_0^2 D_0 / \sigma$ to describe the expansion trajectory of the sheet. In line with those works, Fig. 4(c) shows the same data in Fig. 4(b), but rescaled as $2R_r D_0^{-1} \text{We}_d^{-1/2}$; a factor of 2 is added in the numerator to enable a comparison with Refs. [29,38] where $\dot{R}_0/U \approx 2$ was observed. The speed of \dot{R}_0 used in Fig. 4(c) is determined by a linear fitting of R_r data (following Klein *et al.* [22]) using the first three time delays after the onset of the impact, typically up to 300 ns $\sim 1 \mu\text{s}$. Figure 4(c) shows that the use of We_d successfully collapses all the data, demonstrating that $2R_r D_0^{-1} \text{We}_d^{-1/2}$ can be described by a function depending solely on t/τ_c . For droplet impact on a pillar, such a function was provided analytically in Ref. [29] as $2R_r D_0^{-1} \text{We}_d^{-1/2} = 0.15(t/\tau_c - 0.43)^3 - 0.4(t/\tau_c - 0.43)^2 + 0.12$. This function is depicted in the graph. Wang *et al.* [29] further used this solution of R_r to predict the speed of fragments over the full course of the shedding process. The comparison of $R_r(t)$ to the prediction thereof from Ref. [29], as presented in Fig. 4(c), shows that the sheet expansion in our cases has (i) a larger apex radius $R_{\text{max}} \approx 0.14 D_0 \text{We}_d^{1/2} / 2$ at (ii) an earlier apex moment $t_{\text{max}} \approx 0.38 \tau_c$, and also indicates (iii) a faster initial expansion speed \dot{R}_0 compared to the model (note that the model approximations in Ref. [29] were not aimed at describing the very early time response). These differences may be expected to propagate to the dynamics of the fragment speeds as discussed in Sec. V.

V. FRAGMENT SPEED AND ITS EVOLUTION OVER TIME

A. Determination of fragment speed

The trajectories of the fragments are determined from the shadowgraphy images recorded by the double-frame PCO camera (see the microscopy system details in Fig. 1 of Sec. II). Figure 3(c) illustrates an example of our postprocessing procedure, where we overlap two consecutive images

of the same sheet with a time delay of $\Delta t = 2 \mu\text{s}$. We align both images by overlapping the pixels with the coordinates of the center of the sheet. Black and yellow colors in the image indicate the presence of tin or its absence at both frames, respectively. Green and red colors indicate the presence of tin at either 9 or 11 μs , i.e., at first and second frames, respectively. Using these overlapped images we can keep track of the ballistic trajectory of individual fragments, which we draw using black lines that connect the location of single fragments at two moments in time. Individual fragments that detach from the ligaments acquire a speed that is constant over time. Therefore, the fragment speed u_f can be readily determined by dividing the distance traveled by a single fragment over the preset time interval Δt . To avoid including the fragments that are potentially out of focus and to obviate the need for correcting the finite imaging parallax caused by the 30° front-view angle, we restrict the analysis of the fragments and their positions to a region of interest at the top and bottom of the sheet that comprises $\theta = 90^\circ \pm 10^\circ$ and $270^\circ \pm 10^\circ$, see the white dashed lines in Fig. 3(c). The inset in Fig. 3(c.1) illustrates an example of the detection of a single fragment within this angular range at two moments in time, with its corresponding radial positions plotted in Fig. 3(b). In our measurements, u_f is dominated by its radial component, with the contribution from the azimuthal component accounting for a few percent of u_f . We therefore refer to u_f as the radial speed of the fragments hereafter.

B. Fragment speed versus detachment time

To understand the dynamics responsible for the fragment speeds, we need to establish the origin of the fragments. The fragments are shed from their parent ligaments at a detachment time t_d . Given that the short timescales involved prevent the tracking of the full dynamics of individual ligaments, we determine t_d by individually finding the intersection between the ballistic trajectory of each fragment and the expansion trajectory of the relevant ligaments.

The radial trajectory of the ligaments, R_l , is determined from the distance of the outer contour to the center of the target as was illustrated in Fig. 3(a). Similarly to the analysis of the fragment trajectory, we only consider the outer contour for the region of interest identical to that of the relevant fragments, i.e., comprising $\theta = 90^\circ \pm 10^\circ$ and $270^\circ \pm 10^\circ$, as shown by the dashed white lines in Fig. 3(a). For each image, we take the ligament whose tip is furthest from the center of the target to be most relevant for the subsequent shedding, as these have a high chance to shed fragments. Averaging sufficient images (typically 20 images) taken at one time delay yields the mean value of the instantaneous radial positions of the ligament, which further enables a description of R_l over time. In Fig. 3(b) we plot the expansion trajectory of the ligaments obtained by following this procedure, for the same experimental conditions as those used to obtain the images in Figs. 3(a) and 3(c) ($D_0 = 67 \mu\text{m}$ and $E_p = 20 \text{mJ}$). Both the ligament R_l and rim trajectories R_r show an initial expansion, followed by a gradual decrease of their expansion rate. For each data set of a D_0 - E_p combination, we fit a fourth-order polynomial to the expansion trajectory of the rim R_r with its initial slope matching the corresponding \dot{R}_0 . The results obtained allow us to determine the instantaneous speed of the rim \dot{R}_r [cf. the example case shown in Fig. 3(b)]. For the ligament, we fit an unconstrained third-order polynomial to R_l to describe the continuous change of the position of the ligament tips. From the intersection of the curve for R_l with the fragment trajectory, we obtain the individual detachment time t_d . To gauge the uncertainty in obtaining t_d , we compared taking the instantaneous average ligament length to the instantaneous averaged length of only the outermost ligaments (most relevant for shedding), and found that this choice results in less than a 5% difference in the obtained t_d values.

Figures 5(a) to 5(e) present the fragment speed u_f as a function of the detachment time t_d for different droplet diameters and pulse energies as summarized in Table I. The instantaneous speed of the rim \dot{R}_r is also plotted in Figs. 5(a) to 5(e). We observe that the fragment and rim expansion speed \dot{R}_r monotonically decrease over time. Furthermore, our data illustrate that higher laser energies lead to faster fragment speeds for a given droplet size. At any given detachment time, the speed of the fragments u_f is larger than the instantaneous speed of the rim \dot{R}_r (compare

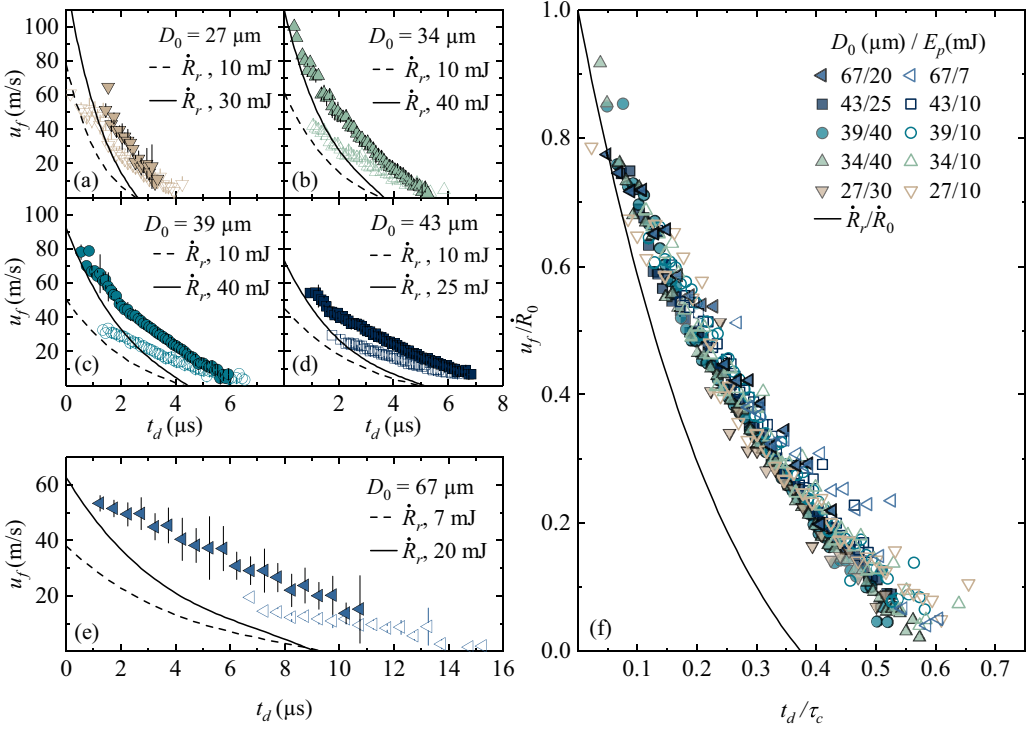


FIG. 5. (a)–(e): Fragment speed u_f as a function of detachment time t_d for the various droplet diameters D_0 . For each droplet size, results obtained using two different laser energies are presented, see Table I. The rim expansion speed \dot{R}_r is also plotted, with solid and dashed lines corresponding to the filled and open symbols, respectively. (f) Same data as presented in (a)–(e), but now scaled by the initial expansion speed of the rim u_f/\dot{R}_0 as a function of the non-dimensional time t/τ_c . The black line presents the non-dimensional speed \dot{R}_r/\dot{R}_0 obtained from a fit of a polynomial to the data in Fig. 4 (c). In (a)–(e) the error bars represent the standard deviation of binned data. These error bars are omitted in (f) for better visibility.

symbols to solid & dashed lines in Fig. 5). This quantitative finding is consistent with the results reported in Refs. [2,29], where the fragment speed is described by a local velocity correlated to the ligament dynamics added to the instantaneous expansion velocity of the rim \dot{R}_r . Our data further indicate that the initial expansion rate of the rim \dot{R}_0 sets the upper limit of the fragment speed during the sheet expansion. With \dot{R}_0 setting the starting point of u_f near $t_d = 0$, the moment at which $u_f = 0$ seems to be solely determined by the initial droplet size D_0 and not by the laser energy E_p . Figures 5(a) to 5(e) show how the time span (from the onset of the impact to the moment when $u_f = 0$) increases as we irradiate a larger droplet. These observations on both the characteristic speed and the timescale of the shedding process inspire us to seek a self-similar solution $y = g(x)$ to explain the fragments' speeds with similarity variables $x = t/\tau_c$ and $y = u_f/\dot{R}_0$, in line with the findings of Wang *et al.* [2]. Figure 5(f) shows the same data presented in Figs. 5(a) to 5(e) but rescaled using \dot{R}_0 and τ_c . The graph indeed reveals a collapse of all data sets onto a single master curve $u_f/\dot{R}_0 = g(t/\tau_c)$. Moreover, as discussed in Fig. 4(c), the scaled evolution of the rim $2R_r D_0^{-1} \text{We}_d^{-1/2}$ can be described by a function that solely depends on $f(t/\tau_c)$, hence one expects a universal solution $\dot{R}_r/\dot{R}_0 = \phi(t/\tau_c)$ where $\phi(x) = \sqrt{3/2} f'(x)$ following the definition of the capillary time and the deformation Weber number. This curve, plotted in Fig. 5(f), is obtained by a concatenated fourth-order polynomial fitting to all the available data of $R_r(t)$ shown in Fig. 4(c). For consistency, the fit is performed with the constraint $\phi(0) = 1$. Due to these two independent collapses of \dot{R}_r/\dot{R}_0 and u_f/\dot{R}_0 , the difference between the rim and the fragment speed scales as

$(u_f - \dot{R}_r)/\dot{R}_0 \sim g(t_d/\tau_c) - \phi(t_d/\tau_c)$, following a function that monotonically increases with time and is independent of the deformation Weber number.

A self-similar behavior of the fragments' speeds was also reported in Refs. [2,29] on droplet impact on a pillar. In those works, the difference in velocities u_f and \dot{R}_r is attributed to (i) the ligament growth and (ii) the speed difference between the tip of ligaments and the fragments due to a one-necking-time shift (also see Appendix B). By using the expansion curve of the rim R_r and by invoking mass conservation associated with the ligament and the rim, Wang *et al.* [29] further analytically identified (i) that $(u_f - \dot{R}_r)/\dot{R}_0$ scales as $We_d^{-3/8}$ and is (ii) almost invariant over time. These two theoretical findings are not supported by our observations, cf. Fig. 5. Moreover, the fragment speeds from Refs. [2,29] may exceed \dot{R}_0 at $t = 0$, where the current study finds that $u_f \rightarrow \dot{R}_r$ when $t_d \rightarrow 0$. We note that the aforementioned description of u_f in Ref. [29] was based on their approximate solution for R_r ; the use of their full solution instead may have led to results that are more in line with the current experimental work. The origin of the discrepancy of the current $(u_f - \dot{R}_r)/\dot{R}_0$ scaling with the pillar impact case [2,29] is yet unclear. A dedicated experimental campaign would be required to be aimed also at the detailed study of the necking process itself. We hypothesize that part of the difference may originate from the very different original impact dynamics, where the laser-impact case has no ‘‘impactor’’ present even on the early, inertial timescale. This difference could cause different initial corrugations of the rim that further propagate to late-time dynamics such as the formation of ligaments and the shedding of fragments [5].

Energy fraction taken by the fragments

Next, we aim to interpret the collapse of the fragment speed onto $u_f/\dot{R}_0 = g(t/\tau_c)$ by considering the energy partitioning. Once the droplet is set in motion by the laser pulse, the initial energy of the droplet E_{tot} can be described by its kinetic energy $\propto M_0(\dot{R}_0^2 + U^2) \sim M_0\dot{R}_0^2$ (as $U \sim \dot{R}_0$) and its surface energy $\propto \sigma R_0^2$, where M_0 is the mass of the original droplet. Given that $We_d \gg 1$ in our experiments, the kinetic energy of the initial droplet is much larger than its surface energy, thus leading to $E_{\text{tot}} \sim M_0\dot{R}_0^2$. The total energy E_{tot} is then distributed across the various channels, such as the sheet, rim, ligaments, and the energy accumulated in the fragments. Wang *et al.* [42] showed, both experimentally and theoretically, that the fraction of the total energy residing in the sheet, rim, and in the fluid shed from the rim (i.e., the sum of ligaments and fragments) was a function of the dimensionless time t/τ_c only and was independent of the Weber number. Inspired by their work, we now further assume that the energy contained in each subsystem is Weber-number independent, including those from ligaments and fragments (E_f) separately, i.e., $E_f/E_{\text{tot}} = h(t/\tau_c)$.

As we will explain below, the cumulative kinetic energy of the fragments can be determined by integration of $\dot{m}_f u_f^2$ over time, where \dot{m}_f is the instantaneous shedding rate of the fragments mass m_f and is also independent of the Weber number. As a result, as we will see, u_f/\dot{R}_0 solely depends on t/τ_c . The relative importance of the kinetic energy of a fragment with a speed u_f and a diameter d_f to its surface energy is captured by the fragment Weber number $We_f = (1/2)(\rho\pi d_f^3/6)u_f^2/(\pi d_f^2\sigma) = \rho u_f^2 d_f/12\sigma$. The value of We_f is then estimated by using the experimental data of u_f from Fig. 5. Following Wang *et al.* [38], d_f is obtained from $d_f \approx 1.7 b_r$ with the diameter of the bounding rim b_r in turn determined from the universal criterion of the local Bond number $Bo = \rho b_r^2(-\ddot{R}_r)/\sigma = 1$, where \ddot{R}_r is the instantaneous deceleration of the rim determined from Fig. 4(c). The relation $Bo = 1$ established in Ref. [25] is based on momentum conservation of the corrugations on the rim, and the relation holds for high-Reynolds-number flows as applicable in our case where the Reynolds number $Re = D_0\dot{R}_0/\nu \sim 10^4$ given the kinematic viscosity $\nu = 0.26 \times 10^{-6} \text{ m}^2\text{s}^{-1}$ of liquid tin [37]. In the present work where the global Weber number $We_d = \rho\dot{R}_0^2 D_0/\sigma$ changes from approximately 1100 to 5500, We_f is significantly larger than 1 at times up to roughly $t/\tau_c \sim 0.4$. Therefore, for those fragments detached at $t_d \lesssim 0.4\tau_c$, the kinetic energy is the dominant contributor to the fragment's energy. The cumulative energy fraction of fragments E_f/E_{tot} at time t is thus given by

$$\frac{E_f(t)}{E_{\text{tot}}} \sim \int_0^t \left(\frac{\dot{m}_f}{M_0} \right) \left(\frac{u_f}{\dot{R}_0} \right)^2 d\tilde{t} \sim h(t/\tau_c). \quad (1)$$

Note that we neglect the (small) onset time of the shedding process and thus the integral in Eq. (1) starts from $t_d = 0$ [29]. It was previously proposed and also experimentally supported in Ref. [38] that for the case of pillar impact, the cumulative mass of fragments is independent of the Weber number and is a function of t/τ_c only. In other words, the term \dot{m}_f/M_0 in Eq. (1) is a function of t/τ_c alone. The instantaneous rate of liquid shed to fragments scales as $\dot{m}_f/M_0 \sim \rho \dot{N}_f d_f^3/M_0$, with \dot{N}_f the instantaneous fragment shedding rate, and d_f the diameter of fragments shed. Given that $\dot{N}_f \sim \text{We}_d^{3/4}$ [38], $d_f \sim D_0 \text{We}_d^{-1/4}$ [24,25,38,42], and $M_0 \sim \rho D_0^3$ we also obtain that \dot{m}_f/M_0 is independent of the Weber number. Therefore, from Eq. (1) we conclude that u_f/\dot{R}_0 is a function of t/τ_c only and is independent of the impact Weber number, consistent with the collapse of all data observed in Fig. 5.

VI. CONCLUSION

Laser pulse impact onto a tin microdroplet leads to an unsteady, fragmenting liquid sheet bounded by a rim. We experimentally determined the speed of fragments u_f that are formed upon breakup of the ligaments protruding from this bounding rim. We observed that fragments are produced by end-pinching for the most of the time interval relevant for the shedding process. In addition, we observed fragments shed via Rayleigh-Plateau breakup of long ligaments at late times. A double-frame camera was used to capture the ballistic trajectories of the fragments, from which their speeds were determined. By finding the intersection of the ballistic trajectory of each fragment and the expansion trajectory of the ligaments R_l , we were able to determine the time of detachment t_d of each fragment. Our data show a monotonic decrease of u_f with t_d . The characteristic detachment time is set by the capillary timescale which depends on the initial droplet size. We observed that the fragment speed is larger than the instantaneous expansion rate of the sheet \dot{R}_r at any given detachment moment t_d . The difference between the fragment and the rim speeds $u_f - \dot{R}_r$ monotonically increases over time, starting from $u_f - \dot{R}_r \rightarrow 0$ when $t_d \rightarrow 0$.

These observations enable us to identify a self-similar behavior, captured by $u_f/\dot{R}_0 = g(t_d/\tau_c)$, which collapses all available data. Such a self-similar behavior, combined with the similarity curve for the sheet expansion speed $\dot{R}_r/\dot{R}_0 = \phi(t_d/\tau_c)$, indicates that the difference in speed between u_f and \dot{R}_r is given by $(u_f - \dot{R}_r)/\dot{R}_0 \sim g(t/\tau_c) - \phi(t/\tau_c)$. The self-similar curves are explicitly independent of the deformation Weber number We_d that was introduced and shown to capture the dynamics of the sheet expansion to a better accuracy than that one offered by the impact Weber number. We further demonstrated that the collapse of u_f is supported by energy conservation arguments, with the assumption that the fraction of the initial energy of the droplet channelled to the fragments is independent of the Weber number. The collapse of u_f enables a model prediction of the instantaneous speed and position of the fragments shed from tin sheets resulting from laser-pulse impact, as employed in state-of-the-art extreme ultraviolet nanolithography. Such a model, requiring as input just the initial droplet expansion speed, would enable the optimization of mitigation strategies against contaminating microparticulate debris to the benefit of the lifetime of industrial lithography tools. The finding that the speed of shed fragments has a robust upper limit of $u_f = \dot{R}_0$ is by itself particularly valuable in this regard. In addition, the correlation found between the rim expansion rate and the fragment speed — covering the full time span of the shedding process — may be applicable to impact scenarios ranging from agriculture, over pathogen transport, to nanolithography.

ACKNOWLEDGMENTS

We thank Alexander Klein for providing the double-frame camera utilized in this study. This work was carried out at the Advanced Research Center for Nanolithography (ARCNL), a public-private partnership of the University of Amsterdam (UvA), the Vrije Universiteit Amsterdam (VU), the Dutch Research Council (NWO), and the semiconductor equipment manufacturer ASML. This project received funding from the European Research Council (ERC) through Starting Grant No. 802648 and is part of the Vidi research program with Project No. 15697, which is financed by NWO.

TABLE I. Parameters including the droplet diameter D_0 , the related capillary time $\tau_c = \sqrt{\rho D_0^3 / (6\sigma)}$, laser pulse energy E_p , and the resulting parameters such as the center-of-mass speed U , initial expansion rate of the sheet \dot{R}_0 , impact Weber number $We = \rho U^2 D_0 / \sigma$, and deformation Weber number $We_d = \rho \dot{R}_0^2 D_0 / \sigma$. Each data entry comprises 20–50 individual laser-droplet events per time delay.

D_0 (μm)	τ_c (μs)	E_p (mJ)	U (m/s)	\dot{R}_0 (m/s)	We	We_d
27	6.5	10	41.5	77.8	583	2091
		30	84.6	126.8	2477	5556
34	9.2	10	33.4	61.3	487	1634
		40	73.1	109.3	2323	5198
39	11.3	10	28.9	50.5	418	1274
		40	62.5	92.2	1949	4240
43	13.0	10	25.4	45.1	355	1122
		25	43.6	72.9	1047	2925
67	25.2	7	19.7	37.9	330	1231
		20	36.6	62.7	1143	3354

APPENDIX A: SUMMARY OF THE EXPERIMENTAL CONDITIONS

To assure the robustness of our experimental results, we systematically study the fragmentation process for five different droplet sizes. For each droplet size, we employ two different laser pulse energies. Experimental details are summarized in Table I.

APPENDIX B: CORRELATION BETWEEN THE FRAGMENT SPEED AND THE SPEED OF LIGAMENTS' TIP

It was found in Ref. [2] that the fragment speed in the laboratory frame follows the velocity of ligaments tip u_l but one necking-time t_{neck} prior to the detachment. In other words, the fragment speed as a function of the detachment time $u_f(t_d)$ relates to the ligament velocity following

$$u_f(t_d) = u_l(t_d - t_{\text{neck}}). \quad (\text{B1})$$

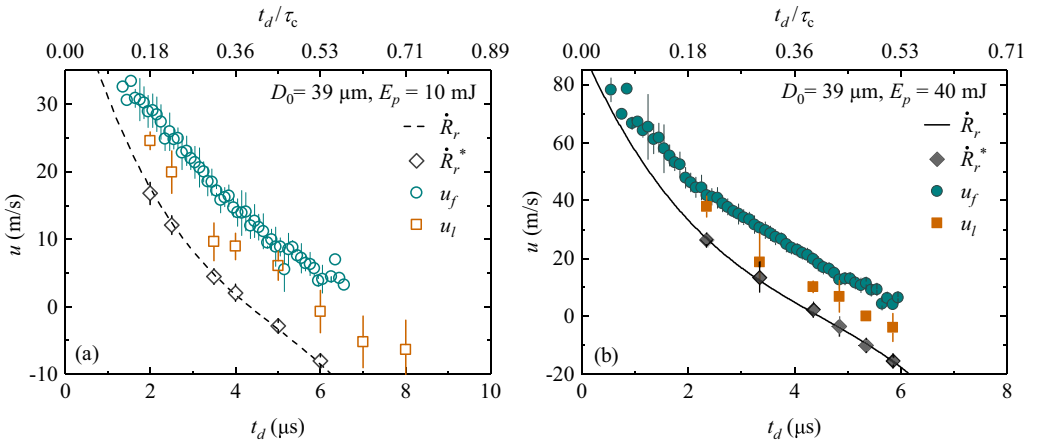


FIG. 6. Speed of fragments u_f and instantaneous velocity of the tip of ligaments u_l as a function of detachment time t_d , along with the expansion rate of the rim \dot{R}_r , \dot{R}_r^* . Two cases with the same droplet diameter $D_0 = 39 \mu\text{m}$ for two laser pulse energies (a) $E_p = 10 \text{ mJ}$ and (b) $E_p = 40 \text{ mJ}$ are presented in the figure.

The necking time $t_{\text{neck}} \sim \sqrt{\rho w_l^3 / \sigma}$ is proportional to the local capillary timescale with the prefactor varying between 2 to 5 (see, e.g., Refs. [2,39,43–45]). This relation yields a t_{neck} ranging from several hundreds of nanoseconds to microseconds in the context of our study where micrometer-thick ligaments are formed.

With the double-frame camera employed in this study, we were able to estimate through visual inspection the speed of a single ligament in the laboratory frame u_l by dividing the traveling distance of the ligament tip by the time delay Δt between the two frames. This method thus provides an average speed of ligaments within Δt . Ligaments speeds u_l obtained following this procedure are presented in Fig. 6 for selected ligaments from the data sets with $D_0 = 39 \mu\text{m}$ at two different energies $E_p = 10 \text{ mJ}$ and 40 mJ that correspond to Figs. 6(a) and 6(b), respectively. Each data point of u_l represents the mean value for typically 10 to 20 manually inspected ligaments in a region of interest identical to that of the fragment speed, i.e., the region comprising $\theta = 90^\circ \pm 10^\circ$ and $270^\circ \pm 10^\circ$. The corresponding fragment speed [i.e., the same data presented in Fig. 5(c)] is also plotted in the graph. Figure 6 shows that the ligament velocity u_l indeed follows the fragment speed, with a temporal shift, ranging from several hundreds of nanoseconds to microseconds, toward earlier moments. Additionally, the distance traveled by the basis of each single ligament, i.e., the local traveling distance of the rim (following the discussion in Sec. IV) can be obtained. These data, labeled as R_r^* to be distinguished from the data set \dot{R}_r , are also presented in Fig. 6. As expected, we observe a close agreement between \dot{R}_r and \dot{R}_r^* , supporting the validity of our procedures to measure both u_l and \dot{R}_r^* .

-
- [1] C. A. E. Peirce, C. Priest, T. M. McBeath, and M. J. McLaughlin, Uptake of phosphorus from surfactant solutions by wheat leaves: spreading kinetics, wetted area, and drying time, *Soft Matter* **12**, 209 (2016).
 - [2] Y. Wang and L. Bourouiba, Unsteady sheet fragmentation: droplet sizes and speeds, *J. Fluid Mech.* **848**, 946 (2018).
 - [3] L. Bourouiba, E. Dehandschoewercker, and J. Bush, Violent expiratory events: on coughing and sneezing, *J. Fluid Mech.* **745**, 537 (2014).
 - [4] B. E. Scharfman, A. H. Tchet, J. W. Bush, and L. Bourouiba, Visualization of sneeze ejecta: Steps of fluid fragmentation leading to respiratory droplets, *Exp. Fluids* **57**, 24 (2016).
 - [5] A. L. Klein, D. Kurilovich, H. Lhuissier, O. O. Versolato, D. Lohse, E. Villermaux, and H. Gelderblom, Drop fragmentation by laser-pulse impact, *J. Fluid Mech.* **893**, A7 (2020).
 - [6] J. Hermens, H. Gelderblom, B. Liu, J. Duffhues, P. Rindt, and O. O. Versolato, Laser-impact-induced splashing: An analysis of the splash crown evolution after Nd:YAG ns-pulse laser impact on a liquid tin pool, *Appl. Phys. B* **127**, 44 (2021).
 - [7] V. Bakshi, *EUV Lithography* (SPIE, Bellingham, WA, 2018).
 - [8] Y. Tao, J. T. Stewart, J. Jur, A. LaForge, D. Brown, M. J. Arcand, A. A. Schafgans, and M. A. Purvis, Extreme ultraviolet light source, ASML Netherlands B.V., US Patent No. 20160007434A1.
 - [9] M. Purvis, I. V. Fomenkov, A. A. Schafgans, P. Mayer, K. Hummler, M. H. Leenders, Y. Tao, S. I. Rokitski, J. Stewart, A. I. Ershov, R. J. Rafac, S. D. Dea, G. O. Vaschenko, D. C. Brandt, and D. J. Brown, Laser-produced plasma incoherent EUV light sources for high-volume manufacturing semiconductor lithography (Conference Presentation), in *Laser-Produced Plasma Incoherent EUV Light Sources for High-Volume Manufacturing Semiconductor Lithography (Conference Presentation)*, edited by A. Klisnick and C. S. Menoni (SPIE, Bellingham, WA, 2019), Vol. 11111.
 - [10] O. O. Versolato, Physics of laser-driven tin plasma sources of EUV radiation for nanolithography, *Plasma Sources Sci. Technol.* **28**, 083001 (2019).
 - [11] T. Sizyuk and A. Hassanein, Tuning laser wavelength and pulse duration to improve the conversion efficiency and performance of EUV sources for nanolithography, *Phys. Plasmas* **27**, 103507 (2020).
 - [12] B. Liu, D. Kurilovich, H. Gelderblom, and O. O. Versolato, Mass Loss from a Stretching Semitransparent Sheet of Liquid Tin, *Phys. Rev. Applied* **13**, 024035 (2020).

- [13] B. Liu, R. A. Meijer, J. Hernandez-Rueda, D. Kurilovich, Z. Mazzotta, S. Witte, and O. O. Versolato, Laser-induced vaporization of a stretching sheet of liquid tin, *J. Appl. Phys.* **129**, 053302 (2021).
- [14] S. Churilov and A. Ryabtsev, Analysis of the spectra of In XII–XIV and Sn XIII–XV in the far-VUV region, *Opt. Spectrosc.* **101**, 169 (2006).
- [15] A. Ryabtsev, É. Y. Kononov, and S. Churilov, Spectra of rubidium-like Pd X–Sn XIV ions, *Opt. Spectrosc.* **105**, 844 (2008).
- [16] G. O’Sullivan, B. Li, R. D’Arcy, P. Dunne, P. Hayden, D. Kilbane, Tom McCormack, H. Ohashi, F. O’Reilly, P. Sheridan, E. Sokell, C. Suzuki, and T. Higashiguchi, Spectroscopy of highly charged ions and its relevance to EUV and soft x-ray source development, *J. Phys. B* **48**, 144025 (2015).
- [17] F. Torretti, J. Sheil, R. Schupp, M. Basko, M. Bayraktar, R. Meijer, S. Witte, W. Ubachs, R. Hoekstra, O. Versolato *et al.*, Prominent radiative contributions from multiply-excited states in laser-produced tin plasma for nanolithography, *Nat. Commun.* **11**, 2334 (2020).
- [18] J. Sheil, O. O. Versolato, A. J. Neukirch, and J. Colgan, Multiply-excited states and their contribution to opacity in CO₂ laser-driven tin-plasma conditions, *J. Phys. B: At. Mol. Opt. Phys.* **54**, 035002 (2021).
- [19] D. Hudgins, N. Gambino, B. Rollinger, and R. Abhari, Neutral cluster debris dynamics in droplet-based laser-produced plasma sources, *J. Phys. D* **49**, 185205 (2016).
- [20] V. Y. Banine, K. N. Koshelev, and G. H. P. M. Swinkels, Physical processes in EUV sources for microlithography, *J. Phys. D* **44**, 253001 (2011).
- [21] I. Fomenkov, D. Brandt, A. Ershov, A. Schafgans, Y. Tao, G. Vaschenko, S. Rokitski, M. Kats, M. Vargas, M. Purvis, R. Rafac, B. La Fontaine, S. De Dea, A. LaForge, J. Stewart, S. Chang, M. Graham, D. Riggs, T. Taylor, M. Abraham *et al.*, Light sources for high-volume manufacturing EUV lithography: technology, performance, and power scaling, *Adv. Opt. Technol.* **6**, 173 (2017).
- [22] A. L. Klein, W. Bouwhuis, C. W. Visser, H. Lhuissier, C. Sun, J. H. Snoeijer, E. Villermaux, D. Lohse, and H. Gelderblom, Drop Shaping by Laser-Pulse Impact, *Phys. Rev. Applied* **3**, 044018 (2015).
- [23] H. Gelderblom, H. Lhuissier, A. L. Klein, W. Bouwhuis, D. Lohse, E. Villermaux, and J. H. Snoeijer, Drop deformation by laser-pulse impact, *J. Fluid Mech.* **794**, 676 (2016).
- [24] E. Villermaux and B. Bossa, Drop fragmentation on impact, *J. Fluid Mech.* **668**, 412 (2011).
- [25] Y. Wang, R. Dandekar, N. Bustos, S. Poulain, and L. Bourouiba, Universal Rim Thickness in Unsteady Sheet Fragmentation, *Phys. Rev. Lett.* **120**, 204503 (2018).
- [26] G. Riboux and J. M. Gordillo, Experiments of Drops Impacting a Smooth Solid Surface: A Model of the Critical Impact Speed for Drop Splashing, *Phys. Rev. Lett.* **113**, 024507 (2014).
- [27] G. Riboux and J. M. Gordillo, The diameters and velocities of the droplets ejected after splashing, *J. Fluid Mech.* **772**, 630 (2015).
- [28] S. T. Thoroddsen, K. Takehara, and T. G. Etoh, Micro-splashing by drop impacts, *J. Fluid Mech.* **706**, 560 (2012).
- [29] Y. Wang, Ph.D. Thesis, Massachusetts Institute of Technology, 2021.
- [30] D. Kurilovich, A. L. Klein, F. Torretti, A. Lassise, R. Hoekstra, W. Ubachs, H. Gelderblom, and O. O. Versolato, Plasma Propulsion of a Metallic Microdroplet and Its Deformation Upon Laser Impact, *Phys. Rev. Applied* **6**, 014018 (2016).
- [31] D. Kurilovich, M. M. Basko, D. A. Kim, F. Torretti, R. Schupp, J. C. Visschers, J. Scheers, R. Hoekstra, W. Ubachs, and O. O. Versolato, Power-law scaling of plasma pressure on laser-ablated tin microdroplets, *Phys. Plasmas* **25**, 012709 (2018).
- [32] J. Hernandez-Rueda, B. Liu, D. J. Hemminga, Y. Mostafa, R. A. Meijer, D. Kurilovich, M. Basko, H. Gelderblom, J. Sheil, and O. O. Versolato, Early-time hydrodynamic response of a tin droplet driven by laser-produced plasma, *Phys. Rev. Research* **4**, 013142 (2022).
- [33] Y. Wang and L. Bourouiba, Drop impact on small surfaces: thickness and velocity profiles of the expanding sheet in the air, *J. Fluid Mech.* **814**, 510 (2017).
- [34] D. Hudgins and R. S. Abhari, Rupture time of droplets impacted by a burst of picosecond laser pulses, *Phys. Rev. E* **99**, 031102(R) (2019).
- [35] Y. H. Jo, I. Jung, C. S. Choi, I. Kim, and H. M. Lee, Synthesis and characterization of low temperature Sn nanoparticles for the fabrication of highly conductive ink, *Nanotechnology* **22**, 225701 (2011).

- [36] J. Lee, W. Shimoda, and T. Tanaka, Surface tension and its temperature coefficient of liquid Sn-X (X = Ag, Cu) alloys, *Mater. Trans.* **45**, 2864 (2004).
- [37] M. J. Assael, A. E. Kalyva, K. D. Antoniadis, R. Michael Banish, I. Egry, J. Wu, E. Kaschnitz, and W. A. Wakeham, Reference data for the density and viscosity of liquid copper and liquid tin, *J. Phys. Chem. Ref. Data* **39**, 033105 (2010).
- [38] Y. Wang and L. Bourouiba, Growth and breakup of ligaments in unsteady fragmentation, *J. Fluid Mech.* **910**, A39 (2021).
- [39] C. Clanet and J. C. Lasheras, Transition from dripping to jetting, *J. Fluid Mech.* **383**, 307 (1999).
- [40] B. Ambravaneswaran, H. J. Subramani, S. D. Phillips, and O. A. Basaran, Dripping-Jetting Transitions in a Dripping Faucet, *Phys. Rev. Lett.* **93**, 034501 (2004).
- [41] T. Driessen, R. Jeurissen, H. Wijshoff, F. Toschi, and D. Lohse, Stability of viscous long liquid filaments, *Phys. Fluids* **25**, 062109 (2013).
- [42] Y. Wang and L. Bourouiba, Mass, momentum and energy partitioning in unsteady fragmentation, *J. Fluid Mech.* **935**, A29 (2022).
- [43] L. Rayleigh, On the instability of jets, *Proc. London Math. Soc.* **s1-10**, 4 (1878).
- [44] R. M. S. M. Schulkes, The contraction of liquid filaments, *J. Fluid Mech.* **309**, 277 (1996).
- [45] S. Gekle and J. M. Gordillo, Generation and breakup of Worthington jets after cavity collapse. part 1. jet formation, *J. Fluid Mech.* **663**, 293 (2010).